7.1 Analysis of Er^{3+}-doped microlasers

The energy levels of Er^{3+} are composed of well separated multiplet, each of which is made up of a number of broadened individual sub-levels. When 1480 nm is the source as pump power, the pump level and upper laser level belong to the same multiplet. Therefore we can use a two level system model to study the systems interaction with the pump and laser fields. The population density in the upper and lower multiplets are N_2 and N_1, respectively. And the total population density is given by $N_T = N_1 + N_2$.

The equation of motion for the pump and signal field can be written as [1-3]:

$$\frac{da_s}{dt} = \left(-\frac{1}{2\tau_s^0} - \frac{1}{2\tau_s^{ext}} + g_s^{Er} \right) a_s \tag{7.1}$$

$$\frac{da_p}{dt} = \left(-\frac{1}{2\tau_p^0} - \frac{1}{2\tau_p^{ext}} + l_p^{Er} \right) a_p + i\kappa_p s \tag{7.2}$$

where a_s and a_p are internal signal and pump fields in the cavity; τ_S^0 and τ_P^0 are the decay time due to the intrinsic loss of the cavity for the laser and pump power, respectively; τ_S^{ext} and τ_p^{ext} are the decay time due to coupling to the fiber taper for the laser and pump power, respectively; κ_p is the field coupling coefficients between the resonator and the waveguide modes at pump wavelength and is equal to $\sqrt{1/\tau_p^{ext}}$; s denotes the input field in the waveguide($|s|^2$ is the input pump power); and g_s^{Er} and l_p^{Er} are the round-trip gain

and loss coefficient for the signal and pump wave, respectively. From the propagation equation of pump and signal fields in the cavity [3], we derive the expression for the intracavity gain and loss coefficients, g_s^{Er} and l_p^{Er}:

$$g_S = \frac{c}{2n_s}\left[\left(\sigma_s^e + \sigma_s^a\right)N_2 - \sigma_s^a N_T\right] \tag{7.3}$$

$$l_p = \frac{c}{2n_s}\left[\left(\sigma_s^e + \sigma_s^a\right)N_2 - \sigma_s^a N_T\right] \tag{7.4}$$

where c is the speed of the light, n_s and n_p are the refractive indices at the signal and pump wavelength, respectively, $\sigma_{s(p)}^e$ and $\sigma_{s(p)}^a$ are the emission and absorption cross section of erbium ions at signal(pump) wavelength, respectively.

At steady state, the time derivatives of the pump and laser field in the cavity are zero, which lead to

$$N_2 = \frac{\frac{n_s}{c}\left(\frac{1}{\tau_s^0} + \frac{1}{\tau_s^{ext}}\right) + N_T\sigma_s^a}{\left(\sigma_s^e + \sigma_s^a\right)} \tag{7.5}$$

$$\frac{a_P}{s} = \frac{i\sqrt{\frac{1}{\tau_p^{ext}}}}{\frac{c}{2n_s}\left[\left(\sigma_s^e + \sigma_s^a\right)N_2 - \sigma_s^a N_T\right] + \frac{1}{2}\left(\frac{1}{\tau_p^0} + \frac{1}{\tau_p^{ext}}\right)} \tag{7.6}$$

7.1.1 Transmission spectrum of the pump

The transmission of the waveguide coupled cavities is [4]:

$$T = \left| 1 + i\kappa_p \frac{a_p}{s_p} \right|^2 \tag{7.7}$$

From equation (7.6) and (7.7), the transmission of the pump power of a fiber taper coupled Er^{3+}-doped microcavity can be written as

$$T = \left| 1 - \frac{\frac{1}{\tau_p^{ext}}}{\frac{c}{2n_s}\left[\left(\sigma_s^e + \sigma_s^a\right)N_2 - \sigma_s^a N_T\right] + \frac{1}{2}\left(\frac{1}{\tau_p^0} + \frac{1}{\tau_p^{ext}}\right)} \right|^2 \tag{7.8}$$

Figure 7.8 shows the transmission of the pump power of a fiber taper coupled Er^{3+}-doped microtoroids. Similar to that of a un-doped cavities, the coupling of the cavity to the waveguide can be divided into three different regimes, which include over-coupled(0<T<1), critical coupled(T=0), and under-coupled regimes(0<T<1).

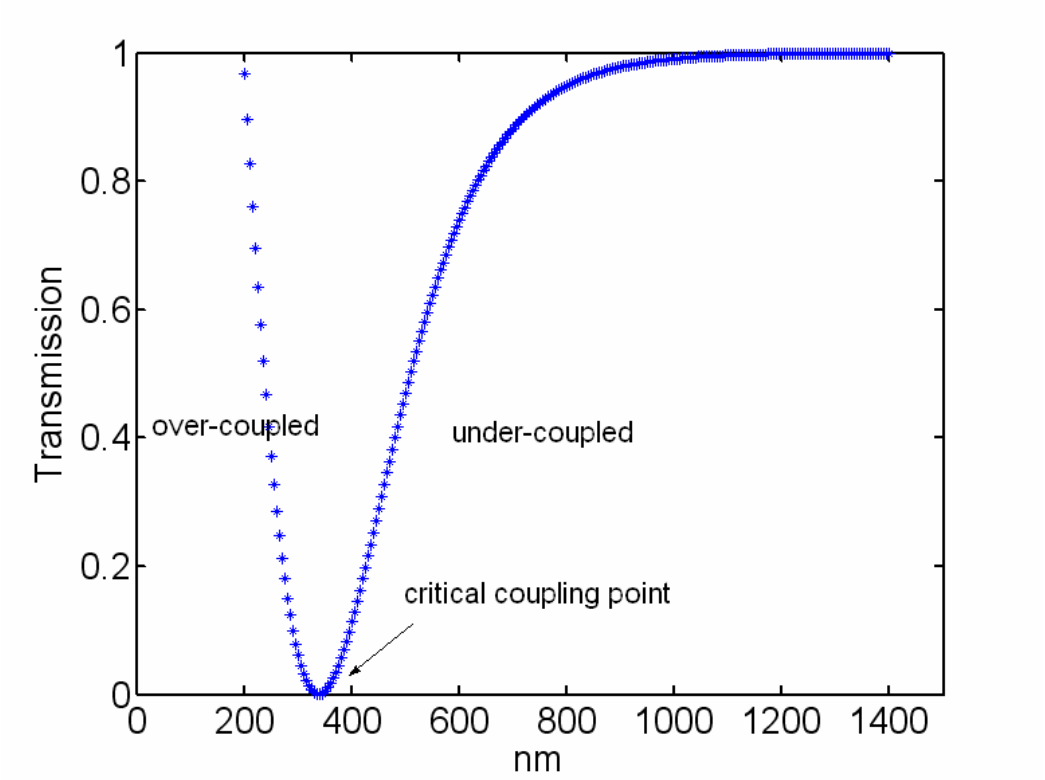

Figure 7.8. Normalized transmission of pump power as a function of air gap between the fiber taper coupler and the microlaser. The diameter of the microlaser is 60 μm. The intrinsic quality factor is 1×10^7.

At zero coupling, no pump power is coupled into the cavity, so this is no laser output power. On the other hand, if we keep increasing the coupling until the cavity is then in the extremely over-coupled regime where no pump power is coupled into the cavity, as a result the laser output power will be zero again. Between those two extreme cases there should exist an optimum coupling condition at which the laser output power is at its maximum. This principal also works for the threshold power and the slope efficiency of the fiber taper coupled cavities

7.1.2 Laser output power of the fiber taper coupled microlasers

The atomic rate equations that describe the population density of levels 1 and 2 in the present of a photon flux of ϕ_s are:

$$\frac{dN_1}{dt} = \frac{N_2}{\tau_{sp}} + (N_2\sigma_e^s - N_1\sigma_a^s)\phi_s + R_{21} \qquad (7.9)$$

$$\frac{dN_2}{dt} = -\frac{N_2}{\tau_{sp}} - (N_2\sigma_e^s - N_1\sigma_a^s)\phi_s + R_{12} \qquad (7.10)$$

where N_1 and N_2 are the population density of level 1 and 2, respectively, R_{21} and R_{12} are the pumping rates into these level, and τsp is the spontaneous lifetime of Er in level 2. Because the lifetime of Er in level 3(~10μ) is much shorter that that in level 2(~10ms), we can assume most of the Erbium stay in level 1 and 2, so $N_1+N_2=N_T$, where N_T is the total population density.

In a steady state situation, we have $\frac{dN_1}{dt} = \frac{dN_2}{dt} = 0$, so we can solve (7.9) to obtain

$$N_2 = \frac{N_T\sigma_a^s\phi_s + R}{\frac{1}{\tau_{sp}} + (\sigma_e^s + \sigma_a^s)\phi_s} \qquad (7.11)$$

where $R=R_{12}=-R_{21}$. The linear gain coefficient g is:

$$g = N_2\sigma_e^s - N_1\sigma_a^s = \frac{N_T\sigma_a^s\phi_s + R}{\frac{1}{\tau_{sp}(\sigma_e^s + \sigma_a^s)} + \phi_s} - N_T\sigma_a^s \qquad (7.12)$$

At steady state, the round trip gain is equal to the round trip loss:

$$e^{gl_0}(1 - L) = 1 \qquad (7.13)$$

where l_0 is the round trip distance and L is the faction of round trip loss. In the case of very small loss(L<<1), so $e^{-gl_0} \cong 1 - gl_0$ and equation (7.13) can be written as

$$gl_0 = L. \qquad (7.14)$$

So at steady state when the pump power exceed the threshold power, the actual gain g felt by the laser oscillation is clamped at the threshold value g_t.

In equation (7.14), replace g with equation (7.12) and the laser photon flux is

$$\phi_s = \frac{1}{L}\left(Rl_0 - \frac{N_T\sigma_a^s l_0}{\tau_{sp}(\sigma_e^s + \sigma_a^s)}\right) - \frac{1}{\tau_{sp}(\sigma_e^s + \sigma_a^s)} \qquad (7.15)$$

where the pumping rate is

$$R = \left(N_1\sigma_a^p - N_2\sigma_e^p\right)\phi_p = \left(N_T\sigma_a^p - N_2\left(\sigma_a^p + \sigma_e^p\right)\right)\phi_p \qquad (7.16)$$

and the round trip loss L is

$$L = \frac{n_s l_0}{c}\left(\frac{1}{\tau_s^0} + \frac{1}{\tau_s^{ext}}\right) \qquad (7.17)$$

with ϕ_p denotes the photon flux at the pump wavelength and the population density N_2 at steady state is given by equation (7.5) . The laser power in the cavity is

$$P_S = Ah\nu_s\phi_s = \frac{V_0 h\nu_s}{L}\left(R - \frac{N_T\sigma_a^s}{\tau_{sp}(\sigma_e^s + \sigma_a^s)}\right) - \frac{Ah\nu_s}{\tau_{sp}(\sigma_e^s + \sigma_a^s)} \qquad (7.18)$$

where A is the cross section area of the laser mode, h is the Plank constant, and v_s is the optical frequency of the laser mode. Figure 7.9 shows the laser output power as a function of the loading condition, i.e. the air gap between the fiber taper coupler and the microlaser, for different intrinsic quality factor. When the intrinsic quality factor of the microlaser is 5×10^6, the maximum laser output power point is in the under-coupled regime and the power drops to zero before the critical coupling point for the pump power. As the intrinsic quality factor increases to 1×10^7, the maximum laser output power point is still in the under-coupled regime, but at the critical coupling point there is still some laser output. If the intrinsic Q increases further, the maximum laser output power point almost overlap with the critical coupling point. It shows that with the increasing intrinsic quality factor Q_0, the maximum laser output point approaches the critical coupling point gradually.

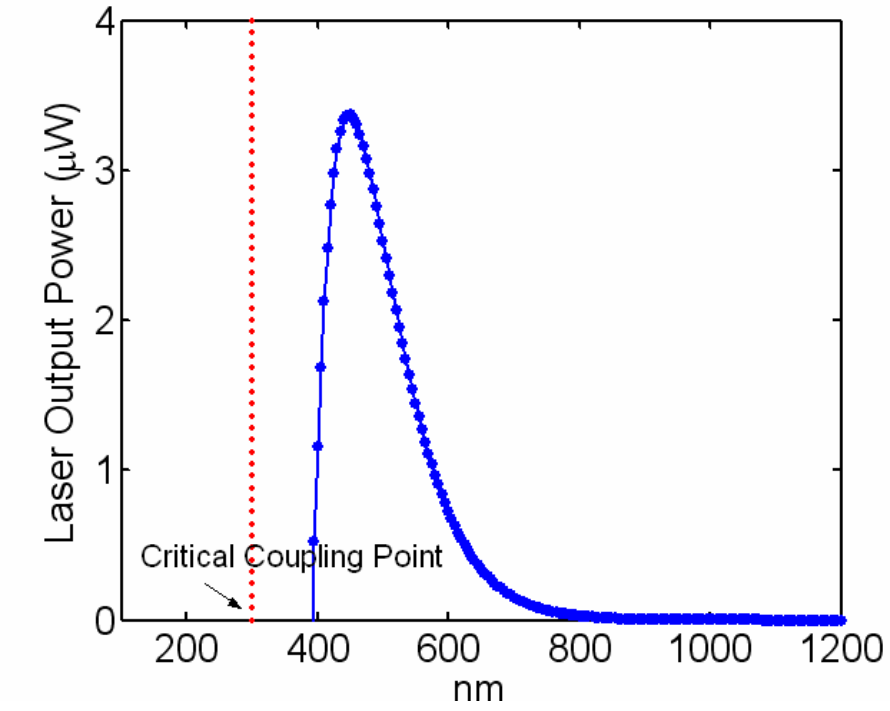
Laser Output Power (μW)
Critical Coupling Point
nm
0
1
2
3
4
200
400
600
800
1000
1200

(a)

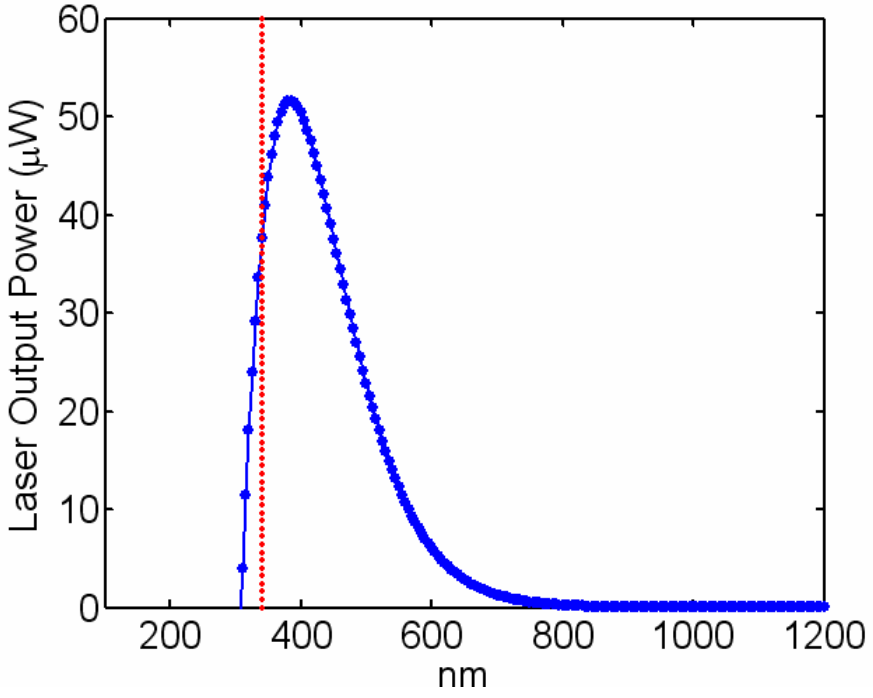
Laser Output Power (μW)
nm
0
10
20
30
40
50
60
200
400
600
800
1000
1200

(b)

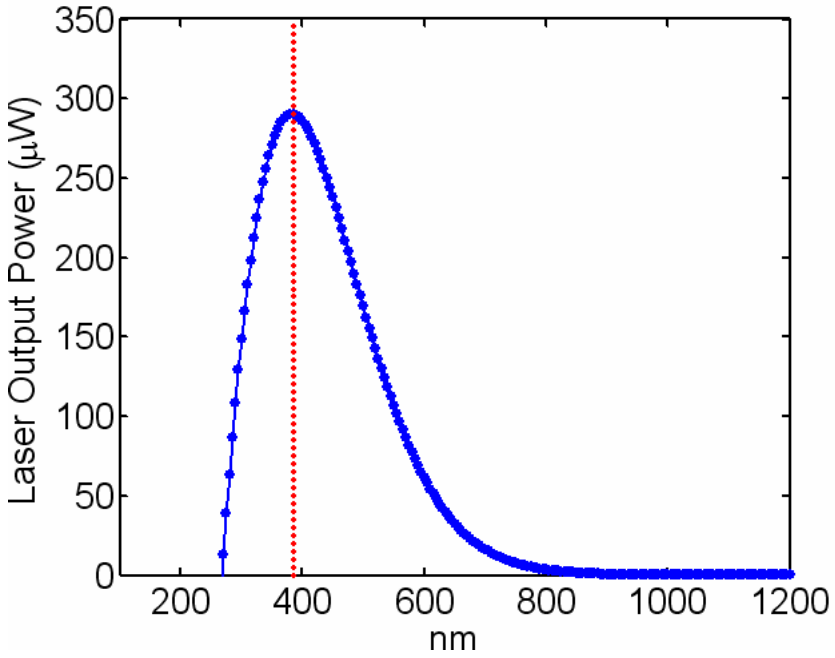

(c)

Figure 7.9. Laser output power as a function of air gap between the fiber taper coupler and the microlasers with different intrinsic Q of (a) 5×10^6 (b) 1×10^7; and (c) 5×10^7. The red dashed line marks the critical coupling point of the pump power.

7.1.3 Threshold power of the microlasers

When pump is at its threshold value, the laser output power is zero. From equation (7.15), the threshold pumping rate is obtained by setting the laser photon flux equal to zero

$$R_{th} = \frac{N_T \sigma_a^s}{\tau_{sp}\left(\sigma_e^s + \sigma_a^s\right)} - \frac{L}{\tau_{sp}\left(\sigma_e^s + \sigma_a^s\right)\gamma_0} \tag{7.19}$$

According the equation (7.16), the pump field in the cavity is

$$\left|a_p\right|_{th}^2 = \frac{\phi_p^{th}}{c} h\nu_p V_p = \frac{R_{th}}{c\left(N_T \sigma_a^p - N_2\left(\sigma_a^p + \sigma_e^p\right)\right)} h\nu_p V \qquad (7.20)$$

The input pump power in the fiber can be calculated from equation (7.6)

$$\left|s\right|_{th}^2 = \tau_p^{ext}\left[\frac{c}{2n_s}\left[\left(\sigma_s^e + \sigma_s^a\right)N_2 - \sigma_s^a N_T\right] + \frac{1}{2}\left(\frac{1}{\tau_p^0} + \frac{1}{\tau_p^{ext}}\right)\right]^2 \left|a_P\right|_{th}^2 \qquad (7.21)$$

And the absorbed pump power can be calculated from equation (7.8) for transmission of the pump power

$$P_{th}^{abs} = \left(1 - T\right)\left|s\right|_{th}^2 \qquad (7.22)$$

Figure 7.10 shows the input and absorbed threshold pump power in the fiber as a function of the air gap between the fiber taper coupler and the cavity. The critical coupling point of the pump is marked by a red dotted line. In the under-coupled regime, when the fiber taper approaches the cavity gradually, i.e. the air gap decreases gradually, the threshold pump power in the fiber decrease gradually because for a given power in the fiber more pump power can be coupled into the cavity. Before the critical coupling point, the threshold pump power in the fiber reaches its minimum value and begins increase when the air gap keeps decreasing. At the critical coupling point, the threshold pump power in the fiber is already much larger than its minimum value. The reason can be that before reaching the critical coupling point, although more input pump power can be coupled into

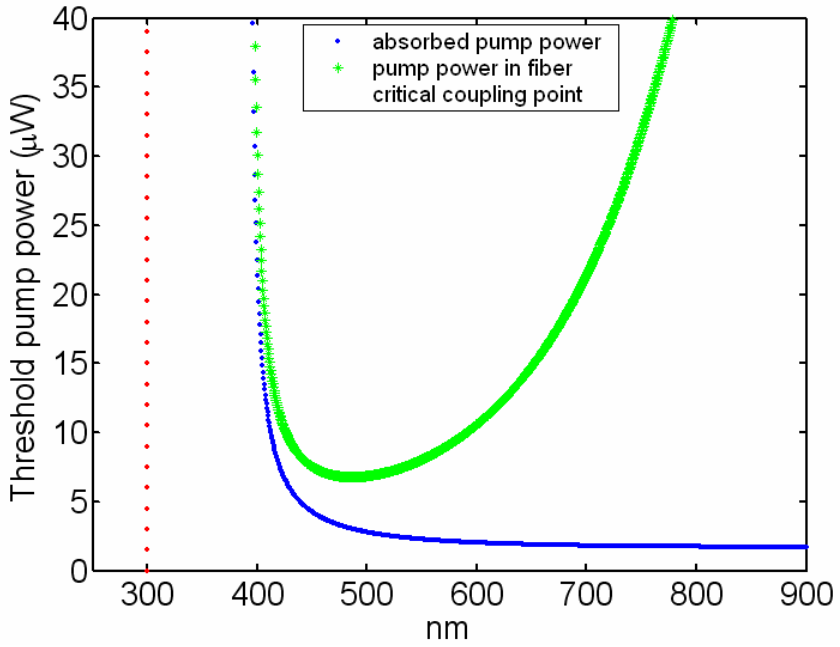
absorbed pump power
pump power in fiber
critical coupling point
Threshold pump power (μW)
nm
0
5
10
15
20
25
30
35
40
300
400
500
600
700
800
900

(a)

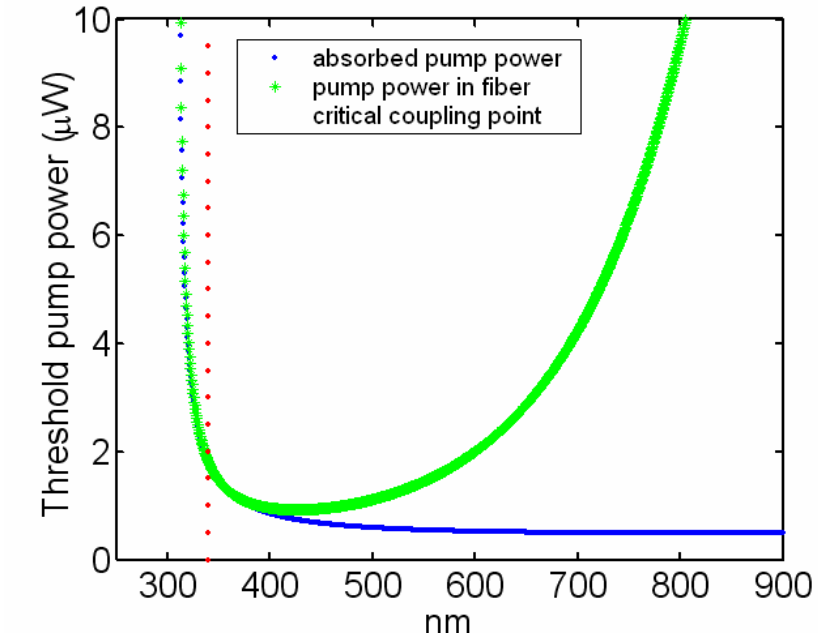
absorbed pump power
pump power in fiber
critical coupling point
Threshold pump power (μW)
nm
0
2
4
6
8
10
300
400
500
600
700
800
900

(b)

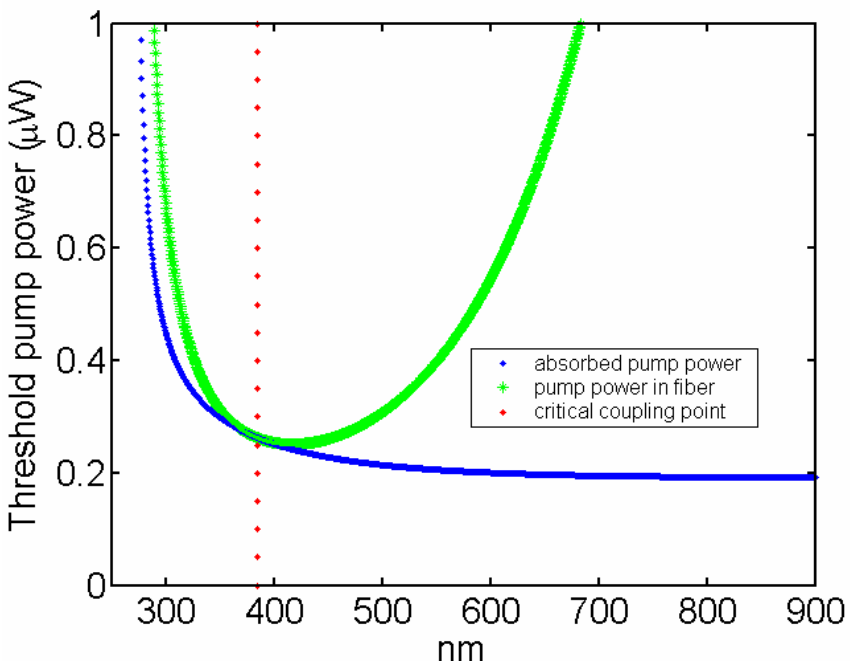

(c)

Figure 7.10. Threshold pump power as a function of air gap between the fiber taper coupler and the microlasers with different intrinsic Q of (a)5×10^6; (b) 1×10^7 ; and (c) 5×10^7. The dashed red line marks the critical coupling point of the pump power.

the cavity when the air gap is smaller, but also more laser power can be coupled out of the cavity which means that the coupling loss for the lasing mode increases, therefore after certain point in the under-coupled region, the effect of increasing coupled pump power can not compensate that of the increasing coupling loss of the lasing mode on the threshold; as a result the threshold increase again. On the other hand, the absorbed threshold keeps increasing when the air gap between the fiber taper and the cavity decreases. For the lasing mode the coupling loss increases monotonically with the decreasing air gap, so the

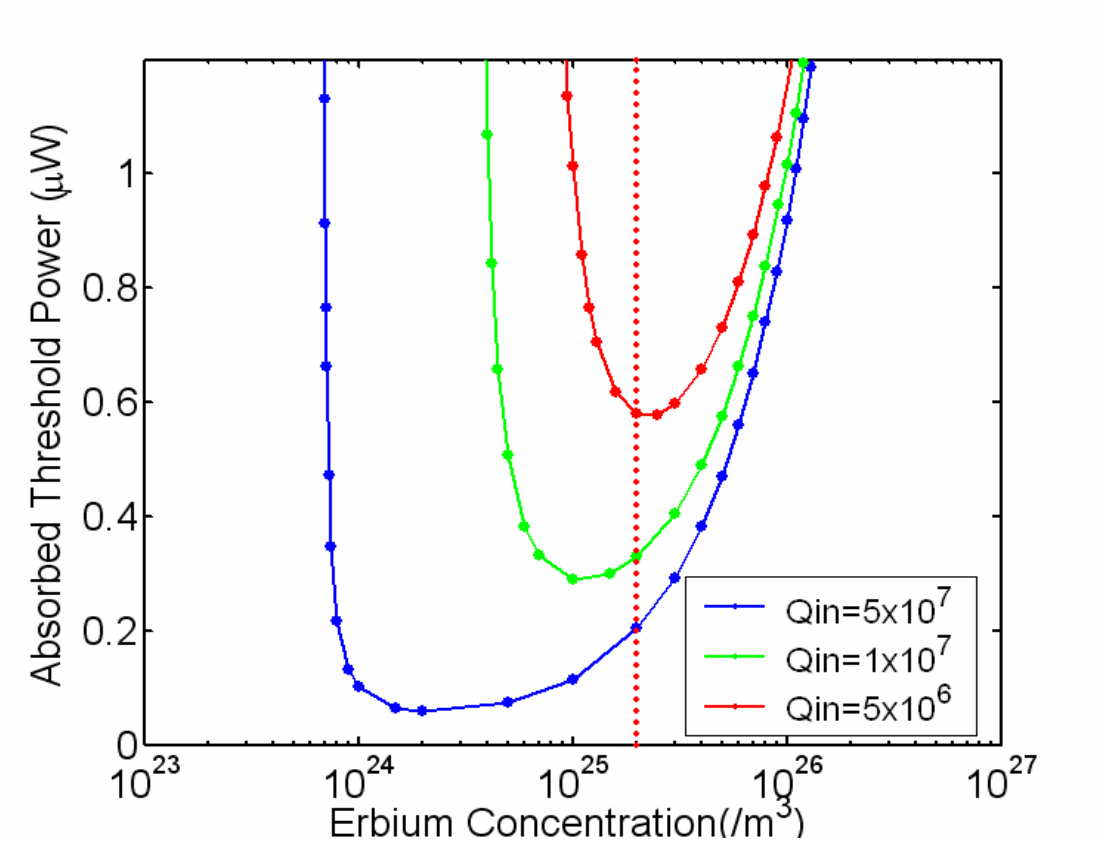

Figure 7.11. Threshold pump power as a function of erbium concentration in the microlasers with different intrinsic Q of (a) 5×10^6; (b) 1×10^7; and (c) 5×10^7. The red dotted line marks the concentration of $2\times10^{19}cm^{-3}$.

minimum absorbed pump power, i.e. threshold, needed to get the laser output increases gradually.

Equations (7.19), (7.20) and (7.21) show that the threshold power also changes with the Er^{3+} concentration in the cavity. Figure 7.11 illustrates the minimum absorbed threshold power as a function the Er^{3+} concentration. It shows that the threshold power is minimized at a certain erbium ion concentration. This optimal erbium ion concentration depends, in turn, on the intrinsic quality factor of the pump mode. In the low concentration limit, the

threshold power increases sharply because Er^{3+} ions are not able to give sufficient gain required for loss compensation; while in high concentration limit, the threshold again increases due to increases of concentration-dependent loss mechanism, such as up-conversion and ion-pairs-induced quenching.

7.1.4 Differential Quantum Efficiency of the microlasers

The differential quantum efficiency of the laser is defined as

$$\eta = \frac{P_{laser}}{P_{pump} - P_{th}} \cdot \frac{v_{pump}}{v_{laser}} \tag{7.23}$$

In sections (7.5.2) and (7.5.3), the laser output power and the input pump threshold have been obtained as the functions of the air gap between the fiber taper and the cavity. Plug those expressions in equation (7.23) and the differential quantum efficiency of the laser as a function of the air gap is presented in figure 7.12. Similar to the case for the laser output power, there is an optimum coupling point where the differential quantum efficiency reaches its maximum value. Compared with the optimum laser output coupling point, the optimum differential quantum efficiency coupling point is at a little more under-coupled point, i.e. larger air gap. It means when the taper fiber approaches the cavity, in general the maximum differential quantum efficiency point will be met first, then the maximum laser output point.

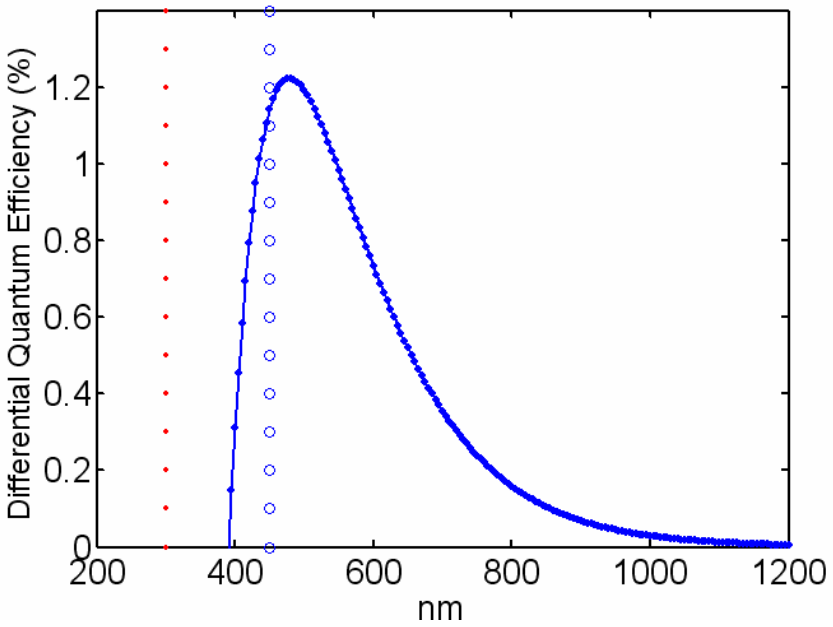
Differential Quantum Efficiency (%)
0
0.2
0.4
0.6
0.8
1
1.2
200
400
600
800
1000
1200
nm

(a)

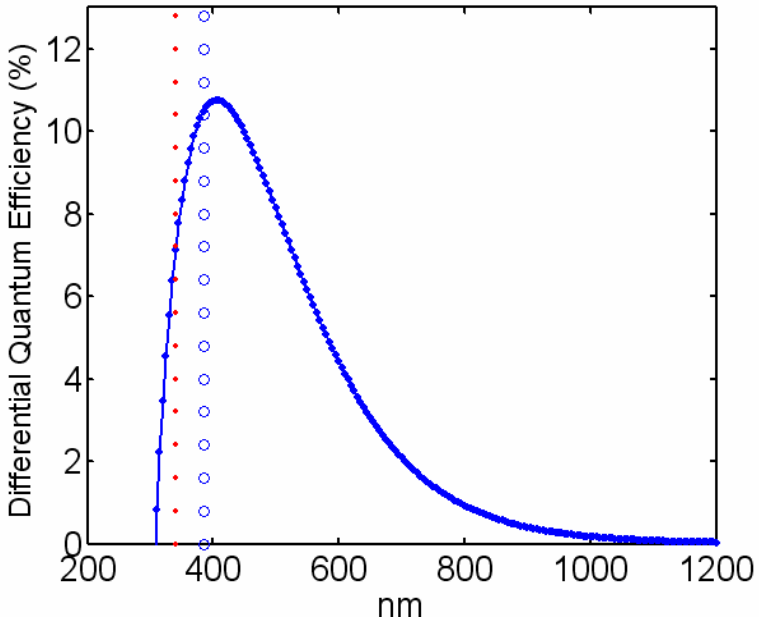
Differential Quantum Efficiency (%)
0
2
4
6
8
10
12
200
400
600
800
1000
1200
nm

(b)

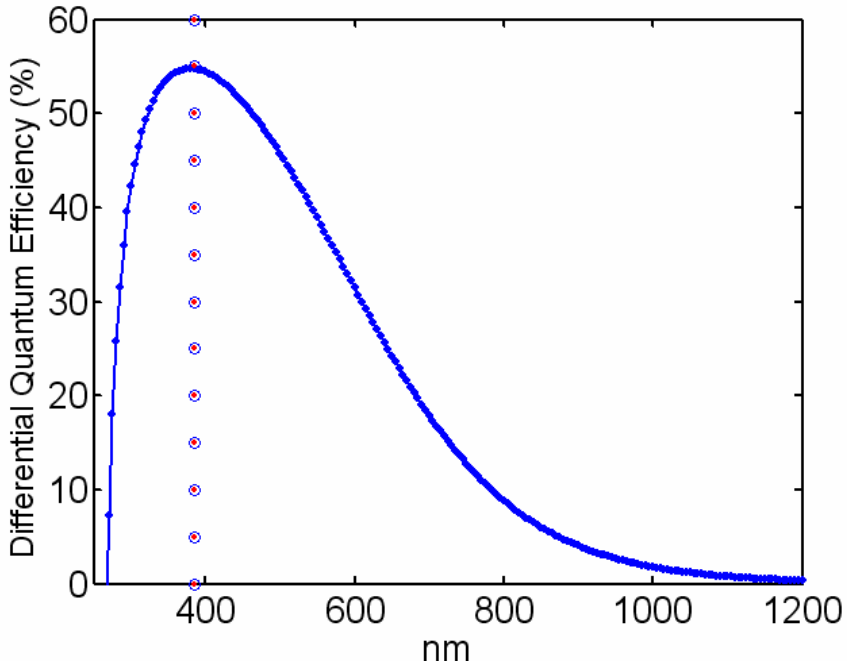

(c)

Figure 7.12. Differential quantum efficiency as a function of air gap between the fiber taper coupler and the microlasers with different intrinsic Q of (a) 5×10^6; (b) 1×10^7; and (c) 5×10^7. The blue and red dotted line marks the maximum laser output point and critical coupling point of the pump mode.

7.1.5 Experimental Results

Er^{3+}-doped microtoroids on a silicon chip were fabricated by the sol-gel method as described in the beginning of this chapter. Different microtoroids were tested and the maximum laser output power always appeared in the under-coupled regime. Figure 7.13 shows the laser output power as a function of the air gap from a microtoroid with diameter of 65 μm and Er^{3+} concentration of 10^{19} cm^{-3}. The differential quantum efficiency versus

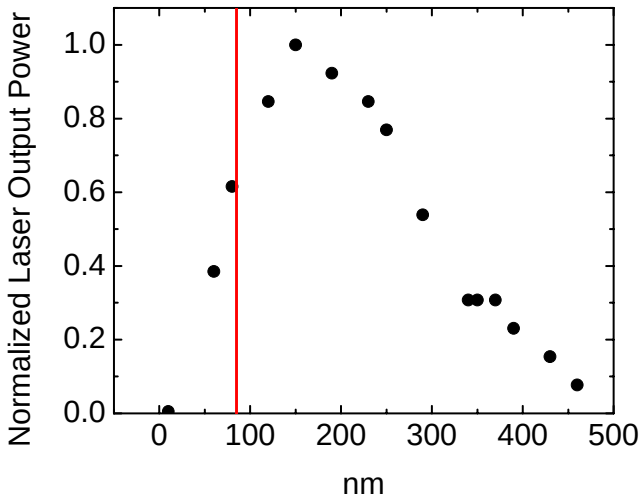

Figure 7.13. Normalized laser output power as a function of air gap between the fiber taper coupler and the microlasers

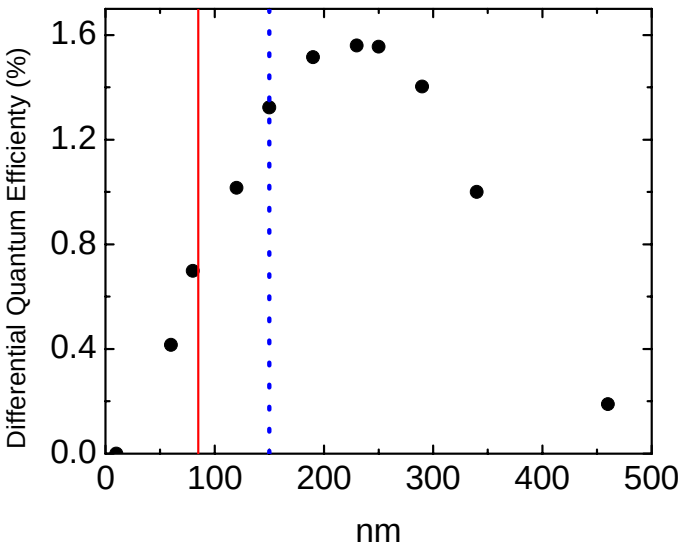

Figure 7.14. Differential quantum efficiency as a function of air gap between the fiber taper coupler and the microlasers

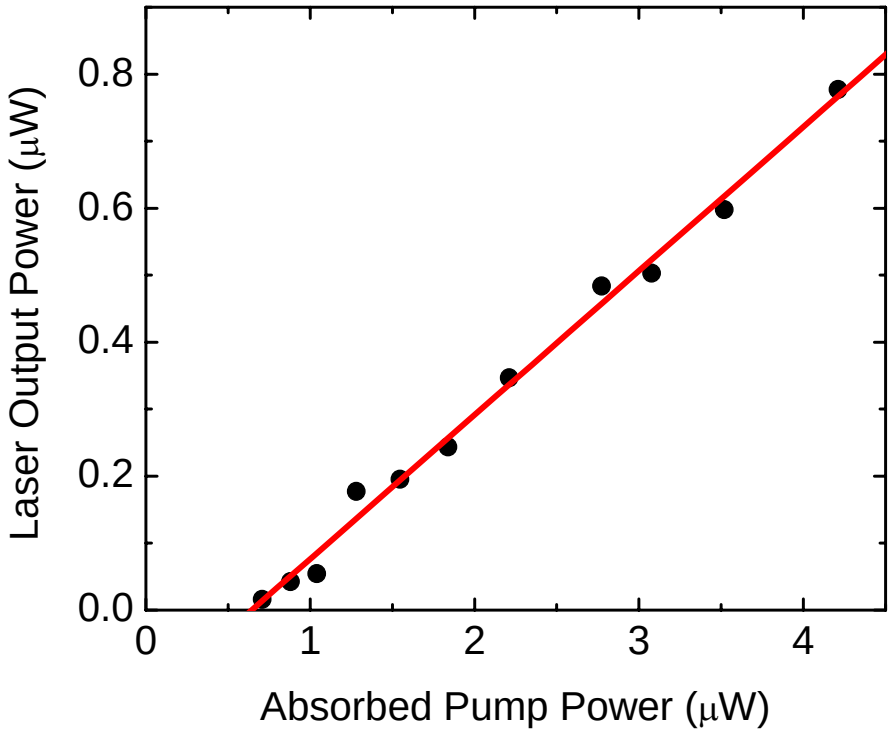

Figure 7.15. Measured laser output power plotted versus the absorbed pump power for a microtoroid laser with principal diameter of 60 μm. The lasing threshold is 660 nW with pump wavelength at 1442 nm and lasing wavelength at 1553 nm.

the air gap is shown in fig. 7.14 with the critical coupling point and maximum laser output power point marked. As the fiber taper get close to the cavity, the pump power coupled into the cavity increases while the coupling loss of the lasing mode also increase, the maximum differential quantum efficiency point is met. When the taper approaches the cavity further, the differential quantum efficiency begins to decrease while the laser output still increases

and reaches its maximum value when it's about 70 nm away from the critical coupling point. The experiment results are consistent with the model derived above. Figure 7.11 shows that a toroid with a principal diameter of 60 μm and intrinsic quality factor (pump mode) between 5×10^6 and 1×10^7, thresholds in the range of 400~600nW can be achieved with an Er^{3+} concentration of 2×10^{19} cm^{-3}. The measured laser output power plotted versus the absorbed pump power from a microtorid with properties as described above is presented in figure 7.15. The threshold was estimated to be as low as 660 nW, which is about three times lower than that of the most recently reported Er-implanted microtoroid resonator [5]. This ultra-low threshold originates from the small mode volume, high quality factor of the microcavity, and homogeneous distribution of the Er^{3+} inside the cavity, which enable the optimized overlap between the active region and the pump modes. Above threshold, the laser output power increases linearly with the absorbed pump power, as expected.

7.2 Conclusion

In conclusion, with the help of both tradition furnace annealing and CO_2 laser-assisted reflow technique, high quality factor microcavities can be fabricated on a Si chip. After the CO_2 laser reflow, a surface roughness within 3 nm can be achieved which enable the very low round trip loss for the microcavities. Without doping inside the silica, a low threshold Raman microlaser can also be achieved. Furthermore, Er-doped silica microlasers can be successfully fabricated from Er-doped sol-gel films and the small mode volume and very low loss of the modes made record threshold in the sub-μW range possible for the Er^{3+}-

doped lasers tested. The analytical model derived for Er^{3+}-doped lasers shows the maximum laser output point is in the under-coupled regime and approaches the critical coupling point of the pump mode as the intrinsic quality factor increases. The maximum differential quantum efficiency point follows the same trend while it is at a more under-coupled point. In addition, the minimum absorbed threshold power for different doping concentration was also investigate to help optimize the doping level to obtain ultra-low threshold microlasers. The results demonstrate the great potential of solgel technology in fabrication of high optical quality materials for integrated optical components on silicon chips.

Chapter 8

PAIRED IONS INDUCED SELF-PUSLING IN ERBIUM-DOPED MICROTOROID LASRES

8.1 Introduction

The dynamics of laser has been an interesting field for investigation since Maiman observed a train of un-damped oscillations in the ruby laser in 1960 [6]. Self-pulsing in laser is interpreted as an intrinsic instability of the laser itself. Different physical origins, such as bidirectional propagation in 'high loss cavity', additional saturable absorber and paired ions, have been observed in some self-pulsing systems [7, 8]. Among them the paired ions induced quenching effect is appropriate for theoretical explanation of self-pulsing operation in heavily Er^{3+}-doped lasers. It has been reported that self-pulsing in erbium-doped fiber lasers is attributed to the existence of ion pairs distributed within the fiber, which is one type of the saturable absorber for the fiber laser system. As the doping concentration increases, the average distance between the ions decrease, which enhance the ion-ion interaction. When both of such ions are in the $^4I_{13/2}$ state, one ion can transfer its energy to the other one, producing one up-converted ion in $^4I_{9/2}$ and one in ground state. Subsequently, the up-converted ion decay rapidly back to $^4I_{13/2}$ state through non-radiatively relaxation. The net effect is loss of one excited ion. For the low paired ion concentration (x<5%, x is the percentage of paired ions), the quenching effect is negligible

and Er^{3+}-doped fiber lasers operate in cw(continuous wave) regime, whereas for high paired ion concentration (x>5%), the lasing is in self-pulsation regime [9].

In this chapter, we develop a model to analysis the self-pulsing operation in Er^{3+}-doped microlasers to understand the mechanism underlying the observed phenomena. In the model, Er^{3+} ions are divided into two groups, single ions and paired ions. Five coupled first-order differential equations are used to describe the dynamical behavior of the system, with two for isolated ions, two for paired ions, and one for the lasing photon. In particular, the pulsation oscillation frequency as a function of the pumping level is studied. The experimental result is presented in the end, which shows consistence with the theoretical prediction.

8.2 Model for ion pairs inducing self-pulsing

As described before, the energy level of Er^{3+} ions are composed of different well-separated levels, each of which is made up of number of individual sub-levels. The isolated ions can be assumed as a three energy level system, which is composed of pumping level, upper laser level and lower laser level. The energy level $^4I_{15/2}$ and $^4I_{13/2}$ are lower laser (ground) and upper laser level, respectively. The pumping level depends on the pump source we use. When the pump wavelength is in the 980 nm band, $^4I_{11/2}$ is the pumping level. For the particular case when 1480 nm laser is used as the pump source, the pumping level and upper lasing level belong to the same energy level $^4I_{13/2}$ with the pumping level (higher sub-level) closer to the top of the level than the upper lasing level (lower sub-

level). Nevertheless, for both cases we can assume that ions in pumping level decay rapidly to the upper laser level through non-radiation relaxation.

Three energy level, ${}^4I_{15/2}$, ${}^4I_{13/2}$ and ${}^4I_{9/2}$, are involved in ion pair interaction [10]. As described in figure 8.1, when both of the neighboring ions are in the ${}^4I_{13/2}$ energy level, ion 1 transfer its energy to ion 2, causing ion 2 up-converted to energy level ${}^4I_{9/2}$ with ion 1 itself relax non-radiatively to ground level ${}^4I_{15/2}$. The up-converted ion 2 quickly decays to the ${}^4I_{13/2}$ energy level through non-radiative relaxation. The net effect of this process is loss of one excited ion, i.e. decrease of population inversion with no contribution to the laser field. The decay time of the paired Er^{3+} ranges from 1 to 100 μs [11]. We use the atomic state of each ion to describe the state of the paired ions so that the atomic state of the paired ions can be written as (α, β), where α and β are the atomic states of the two neighboring ions, respectively. Four states of paired ions contribute to the paired ions interaction and can be written as $({}^4I_{15/2}, {}^4I_{15/2})$, $({}^4I_{15/2}, {}^4I_{13/2})$, $({}^4I_{13/2}, {}^4I_{13/2})$ and $({}^4I_{15/2}, {}^4I_{9/2})$. The decay time of Er^{3+} in level ${}^4I_{9/2}$ relaxes to the lower level much faster than its decay time in level ${}^4I_{13/2}$. As a result, ion in level $({}^4I_{15/2}, {}^4I_{9/2})$ relaxes quickly to $({}^4I_{13/2}, {}^4I_{13/2})$ and we can ignore the population of paired ions in level $({}^4I_{15/2}, {}^4I_{9/2})$. Similar to what we did for the single ions, we

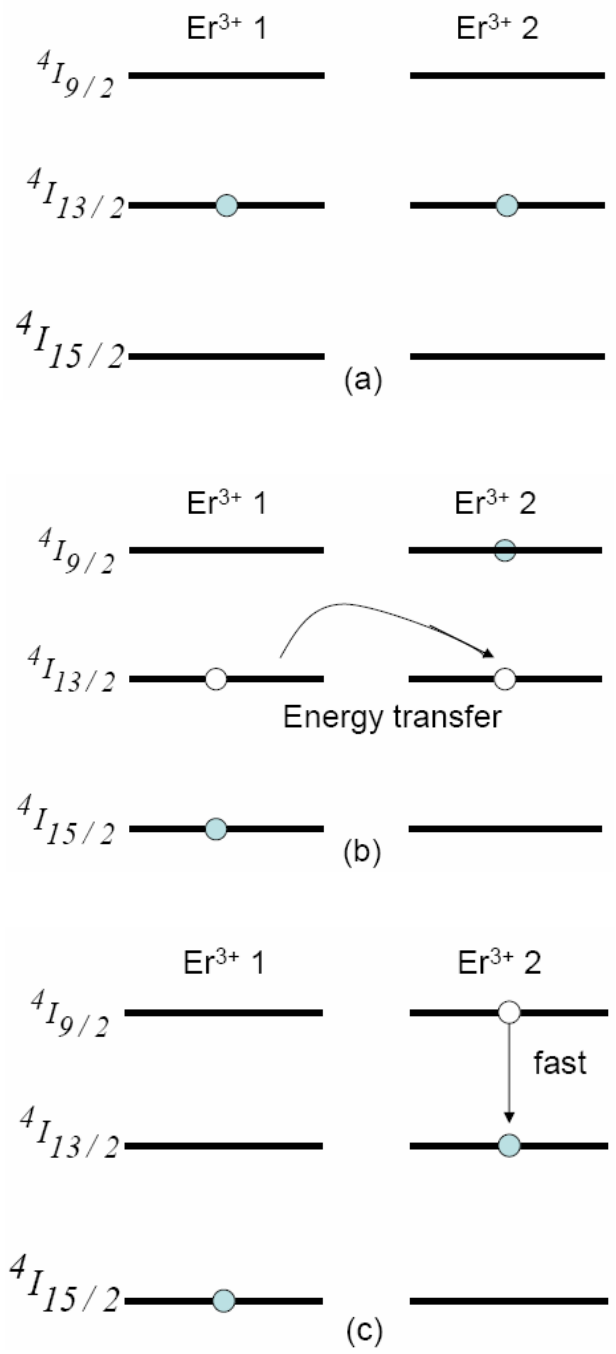

Figure 8.1. Cross-relaxation process between paired ions. (a) two neighboring ions in the $^4I_{13/2}$ level. (b) Energy transfer between two ions. (c)Non-radiative relaxation of ion 1 to $^4I_{15/2}$ level.

describe the paired ions using a three level system as shown in figure 8.2. The $({}^4I_{15/2}, {}^4I_{15/2})$ is called the 0-photon state, where both ions are in the ground state, the $({}^4I_{15/2}, {}^4I_{13/2})$ is called the 1-photon state, where on ion is in the excited state, and the $({}^4I_{13/2}, {}^4I_{13/2})$ is designated as the 2-photon state, where both ions are in the excited state. The decay time of level 2-photon state to 1-photon state ranges from 1 to tens of μs. While for the 1-photon state, one ion is in the ground state and doesn't have cross-relaxation with the other ion, therefore the decay time of 1-photon state to 0-photon state can be assumed to be the same as that of the single ion.

For the single ions, when the ions in ground state are pumped to the pump level, which can be level ${}^4I_{11/2}$ for the 980 nm pump source or a sublevel in ${}^4I_{13/2}$, they relaxes non-radiatively very fast to the meta-stable upper laser level, from where they relaxed to the ground level with emission of one photon through spontaneous emission or stimulated emission. The photons emitted through stimulated emission contribute to the lasing field, while only a small portion of the photons emitted through spontaneous emission can fall into the lasing mode.

According to the analysis of the energy level of the single ions and paired ions above, the rate equations that can be used to describe the dynamical behavior of the Er^{3+}-doped lasers including paired ions are

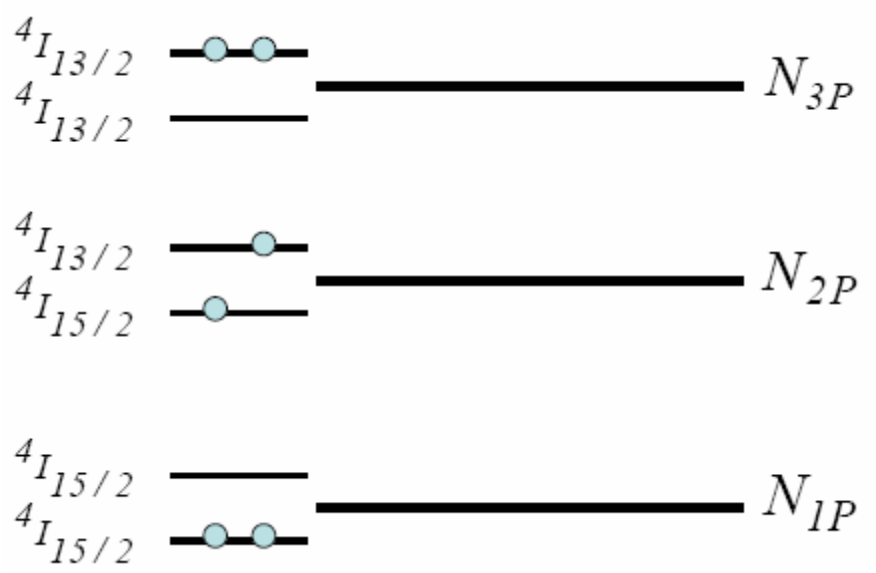

Figure 8.2. Energy level diagram in current model for paired ions

For single ions:

$$\frac{dN_{3S}}{dt} = \left(c\sigma_p^a N_{1s} - c\sigma_p^e N_{3s}\right)P - \frac{N_{3S}}{\tau_{32}}$$

$$\frac{dN_{2S}}{dt} = \frac{N_{3S}}{\tau_{32}} - \frac{N_{2S}}{\tau_{SPS}} - (c\sigma_s^e N_{2S} - c\sigma_s^a N_{1S})\,S$$

For paired ions:

$$\frac{dN_{3P}}{dt} = -(2c\sigma_p^e P + 2c\sigma_s^e S + \frac{2}{\tau_{SPP}})\,N_{3P} + (2c\sigma_p^a P + 2c\sigma_s^a S)\,N_{2P}$$

$$\frac{dN_{2P}}{dt} = (2c\sigma_p^e P + 2c\sigma_s^e S + \frac{2}{\tau_{SPP}}) N_{3P} + (2c\sigma_p^a P + 2c\sigma_s^a S) N_{1P} -$$

$$(2c\sigma_p^a P + 2c\sigma_p^e P + 2c\sigma_s^e S + 2c\sigma_s^a S + \frac{2}{\tau_{SPS}}) N_{2P}$$

For photon density:

$$\frac{dS}{dt} = \gamma \frac{N_{2S}}{\tau_{SPS}} + (c\sigma_s^e N_{2S} - c\sigma_s^a N_{1S}) S - \frac{S}{\tau_{LOSS}} - (2c\sigma_s^a N_{1P} - 2c\sigma_s^e N_{3P}) S$$

The equations above can be used to solve the dynamical behavior of the Er^{3+}-doped lasers. The steady state solution can be obtained by setting the time derivatives of the variables as zero. In these equations, S and P are used to denote the photon density corresponding to the pump and lasing frequency, respectively. The population densities of single ions in the pump level, upper laser level, and lower laser level are labeled N_{1s}, N_{2s}, and N_{3s}, respectively. N_{1P}, N_{2P}, and N_{3P} are the population densities of paired ions in 0-photon state, 1-photon state and 2-photon state. τ_{32} and τ_{SPS} is the lifetime of single ions in pump level and upper laser level, τ_{SPP} is the non-radiative decay time of paired ions from 2-photon state to 1-photon state, and τ_{loss} is the lasing photon decay time in the cavity. σ_p^a and σ_p^e are the absorption and emission cross sections in Er^{3+} for the transition corresponding to the pump frequency, and σ_s^a and σ_s^e are the absorption and emission cross sections in Er^{3+} corresponding to the lasing frequency. c is the speed of light in vacuum. γ is the ratio of spontaneous emission falling into the lasing mode. The

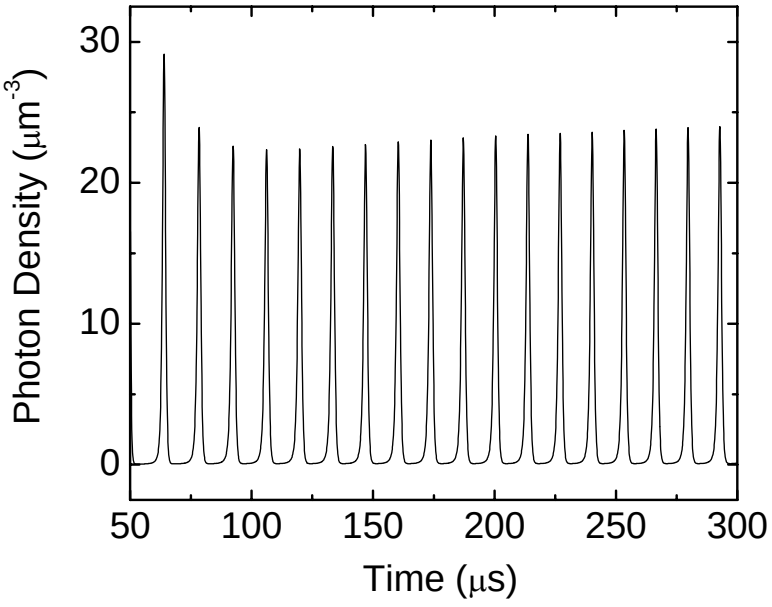
Photon Density (μm-3)
30
20
10
0
50
100
150
200
250
300
Time (μs)

(a)

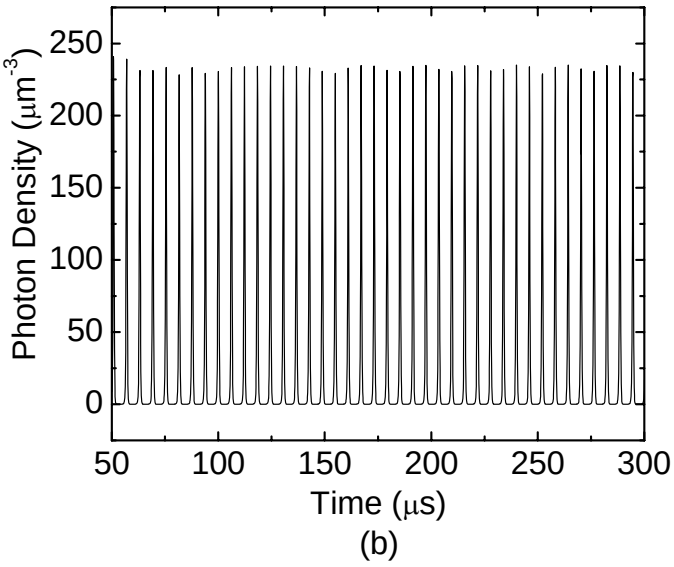
Photon Density (μm-3)
250
200
150
100
50
0
50
100
150
200
250
300
Time (μs)

(b)

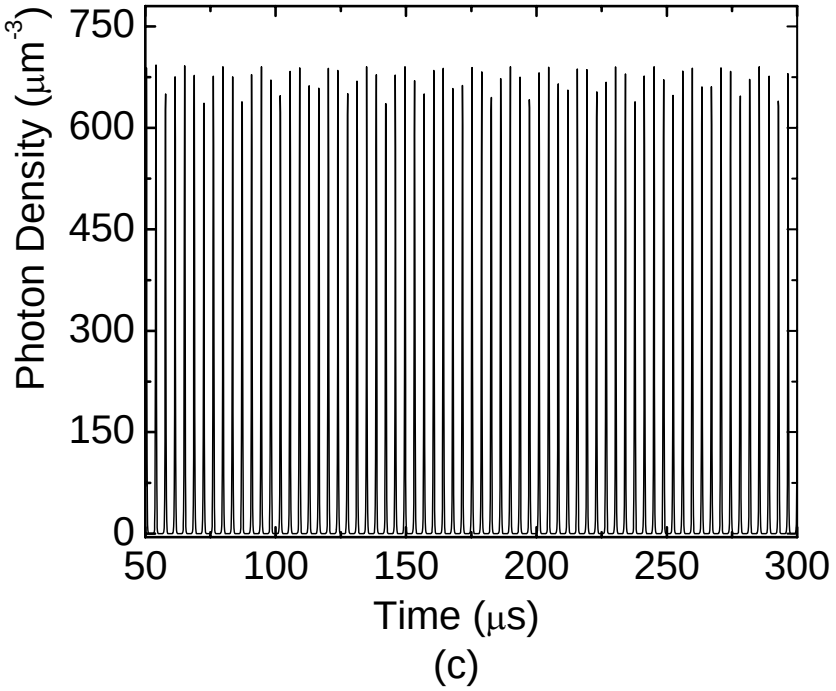

Figure 8.3. Numerical simulation of photon density as a function of time at different pumping level (a) P/Pth=2; (b) P/Pth=8; and (c) P/Pth=20

spontaneous emission factor γ is very small and can be ignored for steady state solution. However, for study of dynamical behavior of the Er^{3+}-doped laser, it's very important to include γ in the system so that the lasing photon density can build up from zero. Dynamical behavior of the Er^{3+}-doped laser is studied with this model. Figure 8.3 gives the numerical simulation of the time evolution of the photon density at different pumping level for the ratio of paired ions being around 10%. The ratio of the pump power to the threshold power is denoted by γ. It shows that self-pulsing oscillation frequency increases with the

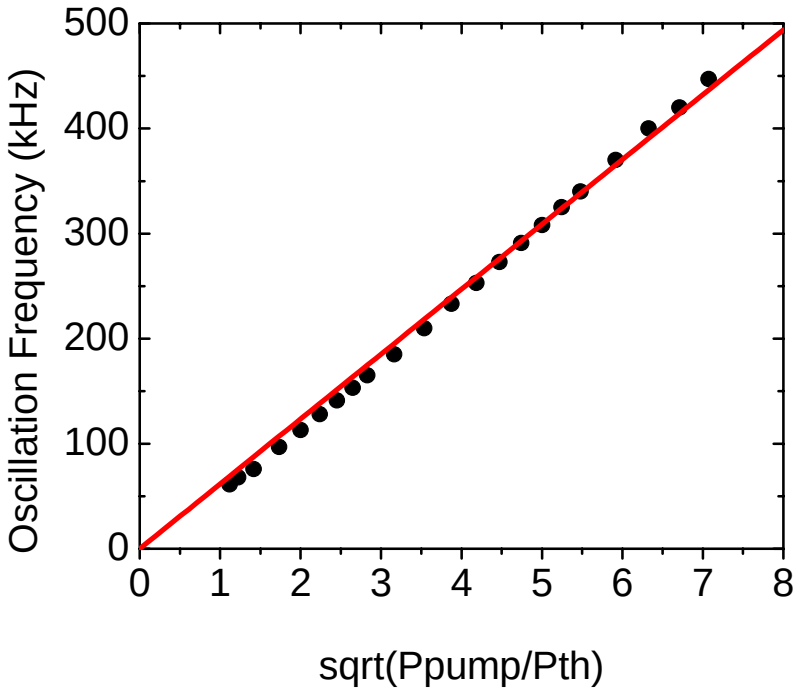

Figure 8.4. Numerical simulation of evolution of the self-pulsing frequency as a function of square root of γ, which is ratio of the pump power with the threshold power

increased pumping level. A linear relation between the oscillation frequency and the square root of γ is presented in Figure 8.4. Table 8.1 list the value of the parameters used for the simulation presented here.

8.3 Experimental results on self-pulsing operation

Table 8.1. Values of parameters used in simulation

Er^{3+} concentration	2.0×10^{19} cm^{-3}
γ: ratio of spontaneous emission captured in laser emssion	1.0×10^{-4}
Absorption cross section of the lasing transition σ_a	6.67×10^{-21} cm^2
Emission cross section of the lasing transition σ_e	7.0×10^{-21} cm^2
Absorption cross section of the pump transition σ_a	6.0×10^{-21} cm^2
Emission cross section of the pump transition σ_a	5.5×10^{-21} cm^2
Upper laser level decay time for single ions τ_{sps}	6 ms
Pump level decay time for single ions τ_{32}	10 μs
2-photo state decay time for paired ions τ_{spp}	10 μs
Photon decay time in cavity τ_{loss}	0.004 μs
Ratio of paired ions K	10%

The influence of the paired ions on the dynamics of the Er^{3+}-doped microtoroid laser has been observed. A tunable single frequency external cavity laser in 1480 nm band is used as the pump source to investigate the dynamical behavior of an Er^{3+}-doped microtoroid laser. Figure 8.5 shows various self-pulsing operation obtained for increasing laser output power, i.e. increasing pumping level. When the laser output is about 1.74 μW, the pulsation frequency is about 578 kHz. When the laser output power increases gradually up to 2.89 μW, a train of pulses with higher frequency of 763 kHz appears. With further increase of the laser output power to 3.71 μW, the self-pulsing frequency reaches 910 kHz. Figure 8.6 shows that the pulsing frequency increases linearly with the square root of the laser output power, which is predicted by the simulation model using paired ions as saturable absorber. As explained before, the lifetime of the paired ions in the 2-photon state is very short, a few

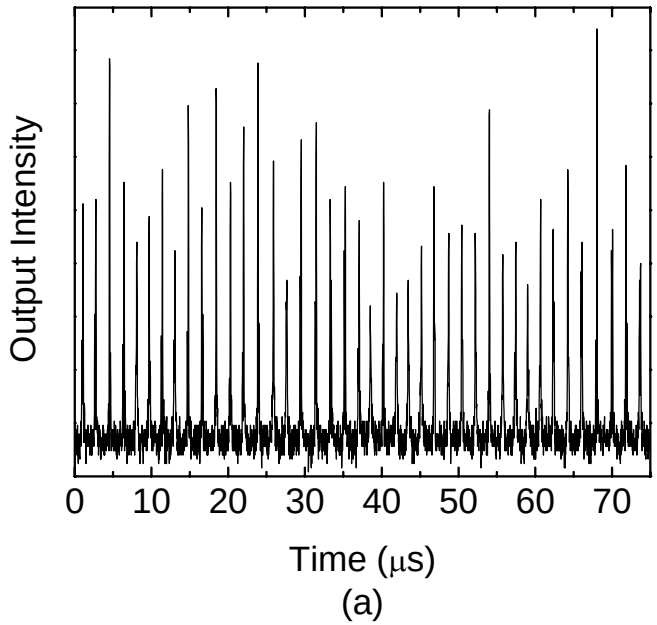
Output Intensity
0
10
20
30
40
50
60
70
Time (μs)

(a)

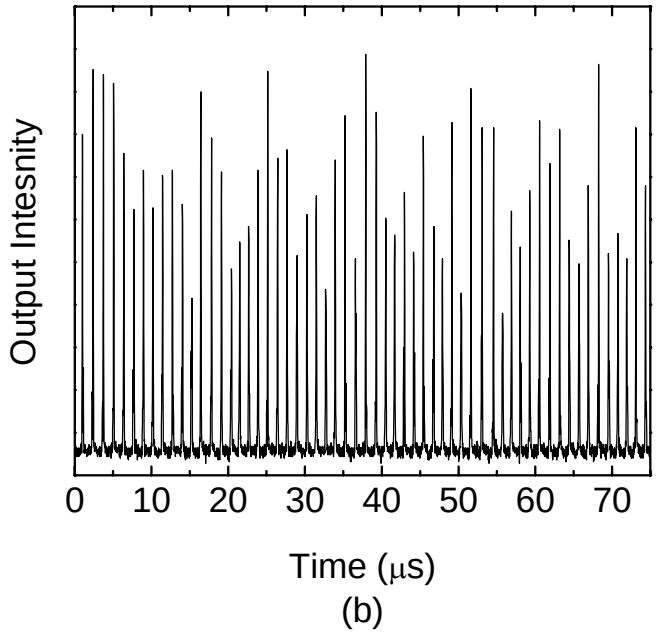
Output Intesnity
0
10
20
30
40
50
60
70
Time (μs)

(b)

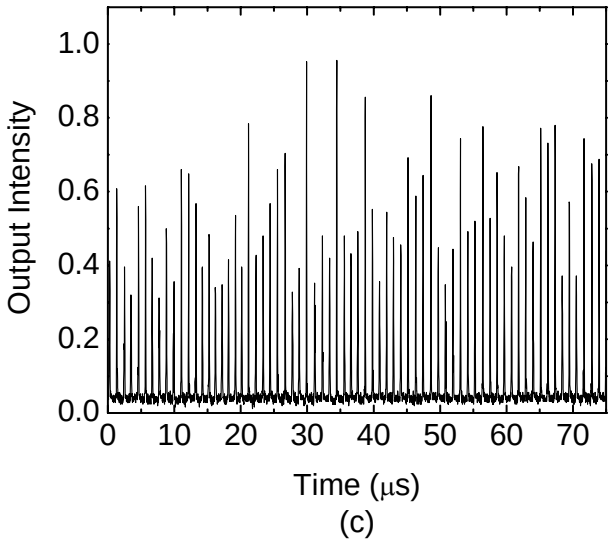

Figure 8.5. Self-pulsing operation of an Er^{3+}-doped microtoroid laser with laser output power of (a) 1.0 μW(b) 1.6 μW and (c)2.1 μW.

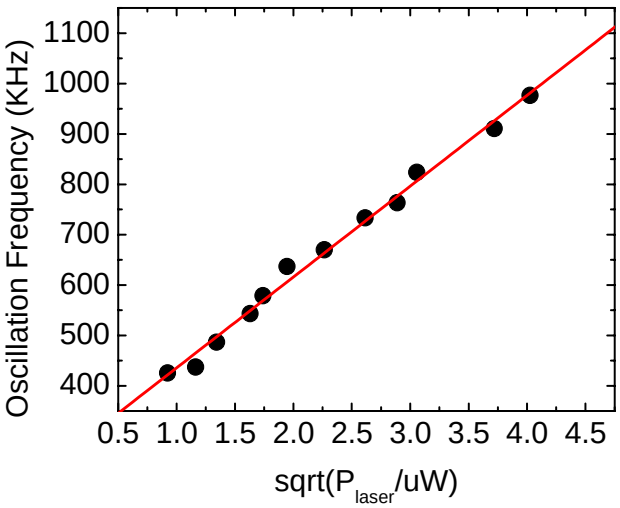

Figure 8.6. Evolution of the self-pulsing frequency as a function of square root of the laser output power. The pump is in 1460 nm band.

μs, so the paired ions may not be sufficiently pumped and act as additional absorber. This saturable absorber make the laser system unstable and thus cause the self-pulsation operation.

8.4 Conclusion

We have shown experimentally and theoretically that self-pulsation operation is possible due to the quenching effect caused by the cross-relaxation between two neighboring excited ions. The time evolution of the laser intensity changes with the pumping level. Furthermore, both the theoretical model and experiments shows that the pulsation frequency increases linearly with the pump power or laser output power. Therefore by varying the doping concentration of erbium in the solgel layers, the laser dynamics can be controlled.

Chapter 9

CONCLUSION AND FUTURE WORK

The research in this thesis presents preparation and characterization of Er^{3+}-doped microsphere lasers and microtoroid lasers on a silicon chip by the sol-gel method. Different schemes are used to gain functionalize different microcavities. For the non-planar structure, microsphere, Er^{3+}-doped sol-gel silica films were deposited outside the microspheres to create gain medium in the microcavities. The same method was also used to surface functionalize the microtoroid cavities on a silicon chip, while in this case due to the unique properties of the microtoroird, only the periphery of the toroids were selectively coated with the sol-gel films. In another method, sol-gel silica is not used just a layer of film outside a given base resonators. Instead, the sol-gel films were deposited on a single silicon chip and toroidal shaped microcavities were fabricated from the sol-gel films directly. It is demonstrated in this work that low threshold Raman microlasers and can be fabricated from un-doped sol-gel silica films and very low threshold Er^{3+}-doped microlasers on a silicon chip can be created from Er^{3+}-doped sol-gel silica films. A continuous lasing with a threshold of 660 nW for Er^{3+}-doped microlaser was also obtained. Furthermore, by varying the Er^{3+} concentration of the starting sol-gel materials, the laser dynamics of the microlasers changes accordingly.

Analytic formulas were derived to predict the laser performance, such as the laser output power, the threshold power, and the differential quantum efficiency, under different loading

condition, i.e. the air gap between the fiber taper coupler and the cavities. In addition, the minimum absorbed threshold power for different doping concentration was also investigate to help optimize the doping level to obtain ultra-low threshold microlaser. The experimental results together with the theoretical analysis give us a better understanding of the laser performance.

By increasing the Er^{3+} concentration in the microcavities, self-pulsing in the microlasers was observed. It is well known that self-pulsing can be achieved with adequate saturable absorber in the laser system. We presented a theoretical model in which we included paired ions as the saturable absorber. It shows that self-pulsing operation can be expected with paired ions induced quenching in the system. The pulsation oscillation frequency increases linearly with the square root of the pumping level, which is consistent with the experimental observation.

The sol-gel method provides a versatile way to fabricate different materials system for various photonics application. It's worthy to exploit their advantages to the maximum in application where they can provide properties not attainable by other methods. There is still a great deal of further work remains to be done.

- Co-doping system in sol-gel materials

As described earlier, more than one dopants can be incorporated in the silica glass by using the sol-gel method. Several co-doping systems can be studied and used to prepare microlasers with better performance:

  - **Yb^{3+}/ Er^{3+}codoping system**

By adding Yb^{3+} and Er^{3+} together into the silica matrix, the pump efficiency of the laser can be increased because the Yb^{3+} has a larger absorption cross section than Er^{3+} and can transfer the energy non-irradiatively to the Er^{3+} to help excite the Er^{3+} to the upper laser level.

- **Al^{3+}/ Er^{3+}codoping system**

Since silica network is built on covalence bond, a certain number of non-bridging oxygen groups must be present to allow for incorporation of Er^{3+}. In pure silica glasses, a rigid structure exists and therefore the amount of non-bridging $Si\text{-}O^-$ is very small. So the solubility of Er^{3+} in the silica network is very low. When the concentration is above certain 'threshold concentration', Er^{3+} tends to aggregate together and form cluster in the silica matrix, which leads to some detrimental effects such as paired ions induced quenching and cooperative up-conversion, etc. When aluminum ions are incorporated into the silica network, they attract the Er^{3+} ions and at the same time increase the number of non-bridging oxygen groups in the silica network. The solubility of Er^{3+} in the silica network is therefore greatly increased.

- Enhanced nonlinear optics sol-gel materials

As mentioned in this thesis work, a low threshold Raman microtoroid laser on a silicon chip can be fabricated from pure silica sol-gel films. On the other hand, silica has a very small Raman gain coefficient. By doping phosphate into the silica network, the Raman gain coefficient can be increase and therefore can further enhance the nonlinear effects in the cavities.

- Low-melting point sol-gel materials

Some applications may involve incorporation of functional organic or biological molecules in the silica network. Densification and reflow at high temperature is avoided in those cases. By using SiO_2/ZrO_2 materials system, the reflow temperature of the sol-gel materials can be decreased as low as 190 °C [12]. This low reflow temperature materials enable incorporation of components which can not sustain high temperature process, such as semiconductor quantum dots, functional organic components or biological components. More application on these materials can be investigated in the future.

- Sol-gel and organic hybrid materials

The introduction of organic components into the silica network permits further tailoring of the chemical and physical properties of the silica glass, such as improved mechanics properties, lower densification temperature, decreased shrinkage during drying and densification etc. For example, by adding photo-sensitive organic components, which can polymerize under exposure to UV light, into the silica network, different degree of exposure to UV light can induce different change of the refractive index in polymerized and non-polymerized region. A grating structure can be created in the sol-gel silica to fabricate new optical devices.

Bibliography

1. Haus H. A., *Waves and fields in optoelectronics*. Prentice-Hall series in solid state physical electronics. 1984.
2. Min B. K., Kippenberg T. J., Yang L., Vahala K. J., Kalkman J., and Polman A., *Erbium-implanted high-Q silica toroidal microcavity laser on a silicon chip*. Physical Review A, 2004. **70**(3).
3. Becker P. C., Olsson N. A., and Simpson J. R., *Erbium-doped fiber amplifiers:fundamentals and technology*. 1999, San Diego: Academic Press.

4. Spillane S. M., Kippenberg T. J., Painter O. J., and Vahala K. J., *Ideality in a fiber-taper-coupled microresonator system for application to cavity quantum electrodynamics.* Physical Review Letters, 2003. **91**(4).
5. Polman A., Min B., Kalkman J., Kippenberg T. J., and Vahala K. J., *Ultralow-threshold erbium-implanted toroidal microlaser on silicon.* Applied Physics Letters, 2004. **84**(7): p. 1037-1039.
6. Maiman T. H., *Stimulated Optical Radiation In Ruby.* Nature, 1960. **187**(4736): p. 493-494.
7. Hideur A., Chartier T., Ozkul C., and Sanchez F., *Dynamics and stabilization of a high power side-pumped Yb-doped double-clad fiber laser.* Optics Communications, 2000. **186**(4-6): p. 311-317.
8. Colin S., Contesse E., LeBoudec P., Stephan G., and Sanchez F., *Evidence of a saturable-absorption effect in heavily erbium-doped fibers.* Optics Letters, 1996. **21**(24): p. 1987-1989.
9. Sanchez F. and Stephan G., *General analysis of instabilities in erbium-doped fiber lasers.* Physical Review E, 1996. **53**(3): p. 2110-2122.
10. Wysocki P. F., Wagener J. L., Digonnet M. J. F., and Shaw H. J. *Evidence and modeling of paired ions and other loss mechanisms in erbium-doped silica fibers.* in *SPIE: Fiber Laser source adn Amplifiers IV*. 1992.
11. Sanchez F., Leboudec P., Francois P. L., and Stephan G., *Effects Of Ion-Pairs On The Dynamics Of Erbium-Doped Fiber Lasers.* Physical Review A, 1993. **48**(3): p. 2220-2229.
12. He M., Yuan X. C., Ngo N. Q., Bu J., and Kudryashov V., *Simple reflow technique for fabrication of a microlens array in solgel glass.* Optics Letters, 2003. **28**(9): p. 731-733.